Journal of MATERIALS RESEARCH

Article
DOI:10.1557/s43578-022-00866-x

EARLY CAREER SCHOLARS IN MATERIALS SCIENCE 2023

ANNUAL ISSUE

Powder metallurgical processing of Al matrix composite reinforced with AlSiCrMnFeNiCu high-entropy alloys: Microstructure, thermal stability, and microhardness

Yagnesh Shadangi[1,2,3,a)], Kausik Chattopadhyay[1], Nilay Krishna Mukhopadhyay[1,a)]

[1] *Department of Metallurgical Engineering, Indian Institute of Technology (BHU) Varanasi, Varanasi 221005, Uttar Pradesh, India*
[2] *Four BK21 Seoul National University Educational Research Division for Creative Global Leaders, Seoul National University, Seoul 08826, Republic of Korea*
[3] *Department of Materials Science & Engineering, Seoul National University, Seoul 08826, Republic of Korea*
[a)] Address all correspondence to these authors. e-mails: yshadangi.met12@itbhu.ac.in; yagnesh.shadangi@gmail.com; yagnesh.shadangi@snu.ac.kr; mukho.met@iitbhu.ac.in mukho_nk@rediffmail.com

Received: 11 June 2022; accepted: 2 December 2022; published online: 5 January 2023

The present work deals with powder metallurgical processing of AA 6082 Al matrix composite reinforced with non-equiatomic AlSiCrMnFeNiCu high-entropy alloy (HEA). The structure, microstructure, morphology, and phase composition of these Al-HEA nanocomposite powders were discerned through XRD and TEM, SEM–EDS, respectively. The AlSiCrMnFeNiCu HEA used as reinforcement was found to have a two-phase microstructure with a major and minor fraction corresponding to the B2-type ($a = 0.29$ nm; cP2) and Cr_5Si_3-type ($a = b = 0.9165$ nm, $c = 0.4638$ nm; tI32) phases, respectively. Mechanical milling (MM) imparts significant refinement, and nanostructuring of grains (~ 10–12 nm) for Al-HEA for nanocomposite powder was observed. These powders of Al-HEA was found to be thermally stable up to 650 ℃. Further, these Al-HEA nanocomposite powders were consolidated through pressure-less sintering at 560 ℃, which led to the formation of a thin ~ 400–500 nm transitional layer at the interface. The microhardness of these Al-HEA composites were tuned in the range of ~ 0.90 to 1.81 GPa.

Dr. Yagnesh Shadangi

Dr. Yagnesh Shadangi (YS) has recently joined the Four BK21 Seoul National University Educational Research Division for Creative Global Leaders, Department of Materials Science and Engineering, Seoul National University, Republic of Korea as Postdoctoral Researcher in ESPark Research Group. Prior to his current position, he worked as Research Staff in the Department of Metallurgical Engineering from January 2021 to September 2022. He received his Bachelor's of Technology in Mechanical Engineering from KIIT University, Bhubaneswar, India in 2010. He then completed his Master's of Technology and Ph.D. in Metallurgical Engineering from Indian Institute of Technology (BHU) Varanasi, India in 2014 and 2020, respectively. He has been recipient of the IIT (BHU) Gold Medal for standing first in M.Tech program, and has attended several national and international conferences in India and abroad. Dr. Shadangi has keen interest in advanced materials processing and its characterization. He has worked on materials like quasicrystals, high entropy alloys, and Al-matrix nanocomposites. His work includes synthesis and materials processing through mechanical milling/ alloying, cryomilling, spark plasma sintering, hot-pressing, vacuum induction melting and vacuum arc melting. He has special interest in materials characterization through X-ray diffraction, electron microscopy, thermal analysis and instrumented indentation techniques.

Introduction

Al-based metal matrix composites (AMCs) have always attracted the attention of researchers and industries due to their enhanced physical and mechanical properties [1]. The properties of the AMCs can be tailored and enhanced by reinforcing them with the suitable reinforcement. These AMCs have better properties than Al and its alloys. The conventional AMCs, are usually reinforced with conventional reinforcements like SiC, Al_2O_3, and nitrides [2, 3]. However, the lack of bonding at the interface between the Al matrix and the ceramic particulates leads to the incoherency between the matrix and reinforcement, acting as a point of stress concentration for generation and propagation of cracks [4]. Further, the exorbitant cost of producing ceramic reinforcement like SiC is almost two to four times more than the price of Al and its alloys [2, 3, 5]. Apart from the cost economics involved, the low toughness, high wear of tools, and recycling of AMCs are highly challenging [2, 3, 5]. For overcoming the issues pertaining to conventional AMCs, a few researchers have fabricated AMCs reinforced graphene having excellent mechanical properties [6, 7]. The interfacial reaction in these AMCs fabricated by severe plastic deformation led to the significant rise in its strength [6, 7]. However, the AMCs reinforced with suitable periodic and aperiodic intermetallics offer good interfacial stability, better room temperature strength and ductility as well as high-temperature strength [8].

In the past two decades, multicomponent high-entropy alloys (HEAs) having five or more principal elements either in the equiatomic, near equiatomic, or non-equiatomic composition have been developed [9]. These HEAs have high hardness, excellent room temperature and high-temperature strength, and good wear and corrosion resistance [10]. The concept of reinforcing AMCs with high-entropy alloys (HEAs) is relatively new [11–20]. In recent years, the HEAs have been exploited as a suitable reinforcement for AMCs due to their enticing microstructural features, strength and thermal stability [12, 19, 21–24]. These AMCs reinforced with HEAs have shown promising results due to interfacial strengthening during processing, fabrication, and heat treatment [12, 19, 21–24].

In 2014, Wang et al. [11] took the initiative to reinforce the 2024 Al matrix with non-equiatomic $FeNiCrCoAl_3$ HEA alloy particles having a single BCC phase. They have processed the AMCs through mechanical milling followed by hot extrusion at a temperature of 773 K. They have reported high strength ~ 710 MPa for 2024 Al matrix reinforced with HEA particles. In an investigation, Kumar et al. [25] reinforced HEA particles in 2024 Al matrix through stir casting with appreciable mechanical properties. In another recent article, Zhang et al. [26] have shown the significant increase in the mechanical properties of 2219 Al matrix reinforced with more than 1.5 wt% of AlCoCrFeNi HEA particles fabricated with unique method of ultrasonic casting technology.

In a study, Tan et al. [22] attempted to reinforce dual-phase HEA particles having FCC and BCC phases into $Al_{65}Cu_{16.5}Ti_{18.5}$ amorphous matrix and consolidated the same by spark plasma sintering (SPS). After SPS, they observed the formation of an inter-diffusion layer between the matrix and the dual-phase reinforcement. The inter-diffusion layer consists of 200–400 nm and is responsible for stable crack propagation during loading. The microstructural features formed during SPS at high temperature were responsible for superior compressive yield strength ~ 3120 MPa for HEA reinforced Al-based amorphous matrix composite. In another study, Karthik et al. [14] attempted to fabricate the layered structure of 5083 Al alloy reinforced with CoCrFeNi HEA (FCC phase with a minor fraction of BCC phase) by friction stir processing (FSP). The FSPed Al-HEA layered composite has the homogeneous and fine distribution of HEA reinforcement in the matrix and no signature of brittle intermetallic due to interfacial reactions. The 5083 Al alloy reinforced with HEA particles exhibits good strength ~ 280 MPa due to the combinations of load transfer and dispersion strengthening mechanisms.

This class of AMCs also offers the formation of an interfacial or transitional layer, which enhances its load-bearing capacity by inhibiting the formation of cracks at the interfaces due to the de-bonding of matrix and reinforcement particles. The formation of the transition layer between the matrix and HEA reinforcement further improves the wettability [11]. These initial studies paved the concept for AMCs reinforced with HEA particles. To date, a few investigations have been conducted to study the AMCs reinforced with HEA particles through pressure-less sintering [27], hot pressing/hot extrusion [16], spark plasma sintering [23], stir-casting [25], additive manufacturing [14], and friction stir processing [28].

In the present work, efforts were made to study the structure, microstructure and morphology, and thermal stability of non–equiatomic AlSiCrMnFeNiCu HEA particles reinforced AA 6082 Al matrix nanocomposite powder milled up to 50 h. Further, the Al-HEA bulk composite was fabricated through pressure-less sintering to study the transitional layer formation arising from the interfacial reaction. The Al-HEA composite's microstructural features and microhardness were investigated through SEM and instrumented indentation technique. This composite has exhibited an appreciable increase in microhardness due to the homogenous distribution of reinforcement and formation of the transition layer at the interface.

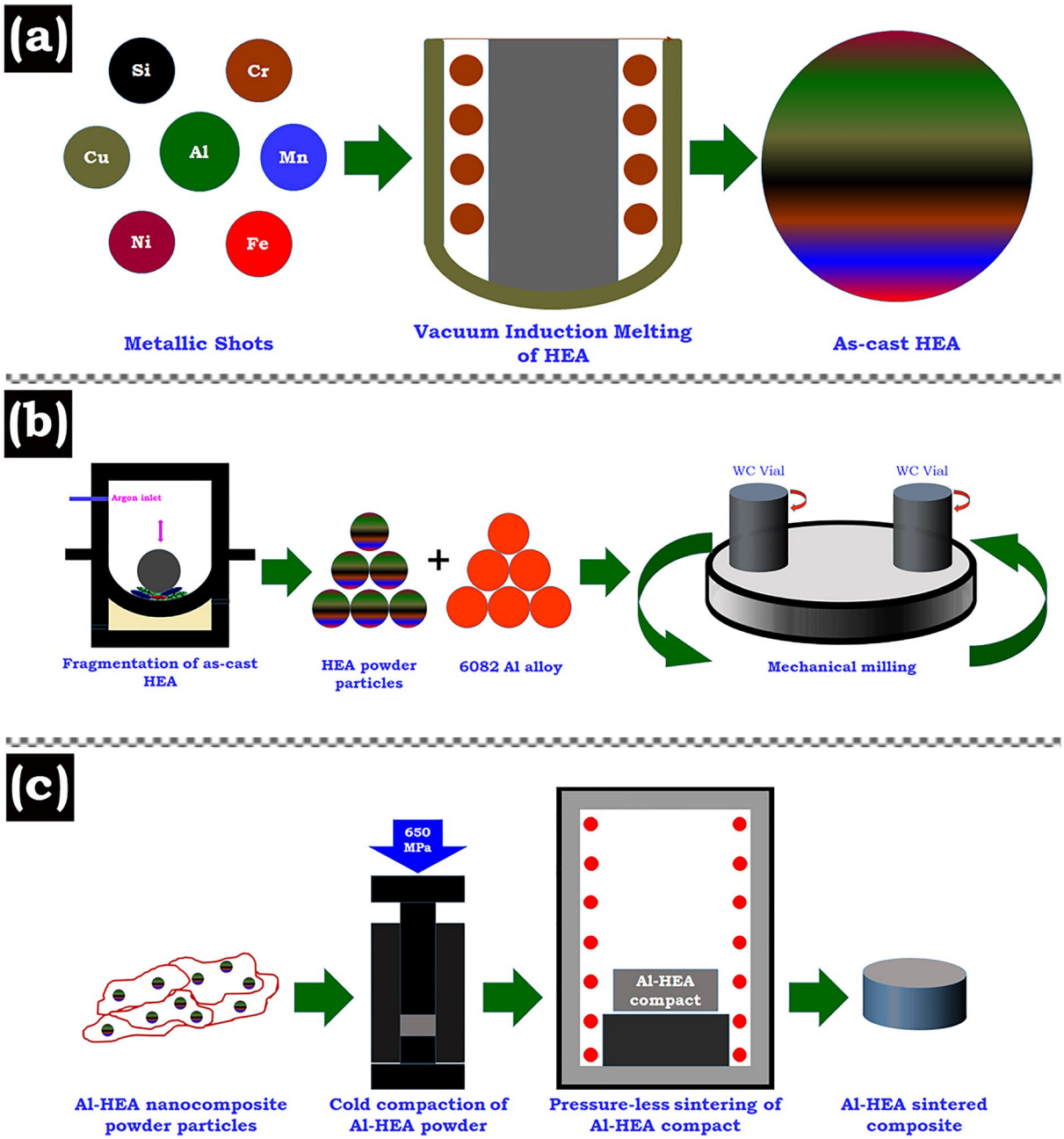

Figure 1: Schematic showing the powder metallurgical processing of Al-HEA composites. (a) Synthesis of as-cast AlSiCrMnFeNiCu HEAs; (b) Synthesis of Al-HEA nanocomposite powders through mechanical milling; (c) Preparation of bulk Al-HEA composites through pressure-less sintering.

Results

The as-cast non–equiatomic AlSiCrMnFeNiCu HEA has a density of 5.08 g cm^{-3}. The schematic of Al-HEA composite fabrication is shown in the Fig. 1 and details are mentioned in the 'Experimental Details'. The detailed phase analysis, morphology, and nominal composition of the as-cast and powdered HEA were discerned through XRD and SEM–EDS, as shown in Fig. 2. The phases formed in the as-cast non-equiatomic AlSiCrMnFeNiCu HEA powder particles are represented in [Fig. 2(a)]. The non-equiatomic HEA prepared by vibratory milling of as-cast samples will be referred to as HEA for simplicity. It is clear from [Fig. 2(a)] that the as-cast HEA contains two types of phases, i.e., a major phase corresponding to the B2-type and a minor phase corresponding to the Cr_5Si_3. The major phase have all the reflections (i.e., (100), (110), (111), (200), (210), (211)) corresponding to the B2-type (AlFe) phase (PDF card no.: 65-3201; $a = 0.29$ nm; cP2; $Pm\bar{3}m$). The minor phase have all intense reflection (002) ($d \sim 0.231$ nm), (321) ($d \sim 0.222$ nm), (411) ($d \sim 0.2004$ nm),

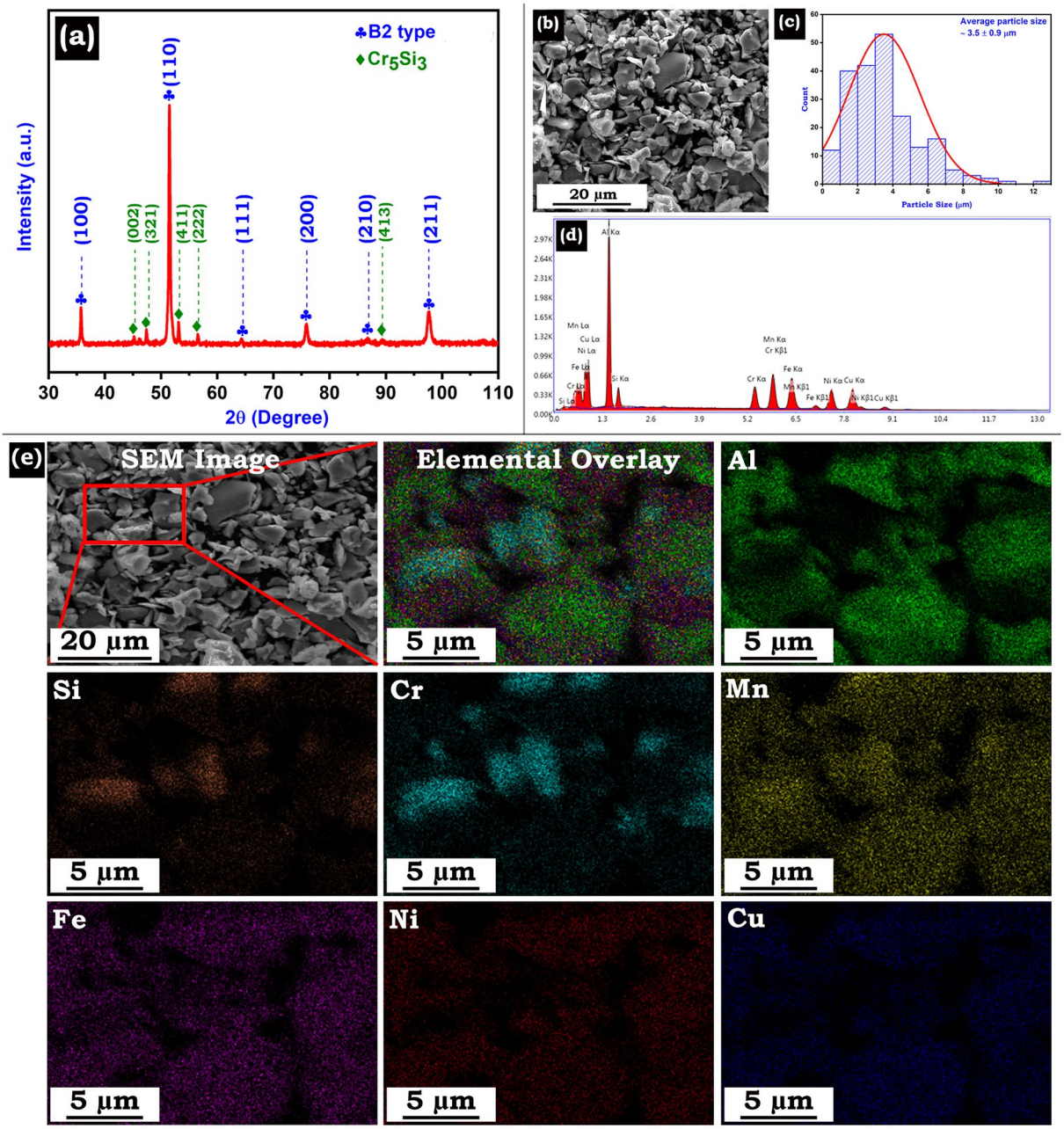

Figure 2: (a) Phase analysis of as-cast non-equiatomic HEA powders prepared by vibratory milling; (b) SEM micrograph showing the morphology of as-cast HEA particles; (c) Particle size distribution of HEA powder particles; (d) EDS spectrum of as-cast HEA sample. (e) SEM–EDS elemental mapping showing the distribution of alloying elements along with the presence of Cr, Si-rich region in as-cast non-equiatomic AlSiCrMnFeNiCu HEA powder particles.

(222) (d ~ 0.1885 nm), (413) (d ~ 0.126 nm) confirming the tetragonal Cr_5Si_3 (PDF card no.: 00-051-1357; $a = 0.9165$ nm, $c = 0.4638$ nm; tI32; I4/mcm).

The morphology of the as-cast powdered HEA particles used as a reinforcement in the AMCs is shown in [Fig. 2(b)]. The as-cast HEA fragmented by milling forms the powdered HEA particles through cleavage fracturing as evident from the faceted morphology after milling at a BPR of 100:1. The cleavage fracture in such materials is a normal phenomenon due to their high hardness and inherent room temperature brittleness. Figure 2(d) shows the particle size distribution of the powdered HEA particles prepared after 30 min of milling. The average particle size was found to be ~ 3.5 ± 0.9 μm. Further, the EDS spectrum of powdered HEA particles is shown in [Fig. 2(d)], and nominal composition of as-cast HEA is mentioned in Table 1. It is evident from the EDS spectrum that as-cast powdered HEA

TABLE 1: Elemental composition of as-cast non-equiatomic AlSiCrMnFeNiCu HEA and physical properties of alloying elements.

Elements	Al	Si	Cr	Mn	Fe	Ni	Cu
Desired composition	40	10	10	10	10	10	10
Final composition	36.2	8.8	10.9	10.3	11.8	10.3	11.2
Physical properties of alloying elements in non-equiatomic HEA							
	Elements						
Parameter	Al	Si	Cr	Mn	Fe	Ni	Cu
Self-diffusion coefficient (m^2/s)	10^{-19}	10^{-62}	10^{-41}	10^{-36}	10^{-31}	10^{-37}	10^{-27}
Thermal conductivity (W/m K)	238	139	91	8	78	89	397

particles show all the alloying elements without any prominent signature corresponding to oxygen. However for Al, minor loss is apparent and can be attributed to the evaporation during melting at high temperatures (Table 1).

The SEM–EDS elemental mapping of as-cast powdered HEA is shown in [Fig. 2(e)]. The elemental distribution of the alloying elements used to synthesize as-cast HEA is evident in [Fig. 2(e)]. From the SEM–EDS analysis, two distinctive regions, lean and rich in Cr and Si, were evident. It can be discerned from [Fig. 2(e)], that those regions showing high-intensity corresponding to the Cr and Si have low intensity corresponding to the other elements like Al, Fe, Ni, and Cu. Similarly, the area with high-intensity corresponding to the elements like Al, Fe, Ni, and Cu shows very low intensity for Cr and Si. Further, it was observed from the SEM–EDS mapping that the intensity of Mn was found to be uniform suggesting its homogenous distribution.

The Al-HEA nanocomposite powder was prepared by mechanical milling (MM) up to 50 h with the varying volume fraction of HEA particles. Detailed phase analysis by XRD was done to ascertain any structural transformation of either Al matrix or HEA reinforcement during 50 h of MM. The phase analysis of Al-10HEA, Al-20HEA, and Al-30HEA nanocomposite powder was shown in [Fig. 3(a)–(f)], respectively. It was observed that even after varying the volume fraction of reinforcement from 10 to 30 vol%, no changes in the Al matrix were detected. During MM up to 50 h, starting AA 6082 Al matrix shows the presence of all reflections of FCC-Al ($a = 0.40494$ nm), i.e., (111), (200), (220), (311), and (222). During milling of Al-HEA nanocomposite powder, no structural transformation of the B2-type major and Cr_5Si_3-type minor phases was observed, as illustrated in [Fig. 3(a)–(f)]. Figure 3(b), (d), and (f) show the enlarged image representing the co-existence of Al-matrix, B2-type phase, and Cr_5Si_3-type phase for Al-10HEA, Al-20HEA, and Al-30HEA, respectively. Even after MM for 50 h, the B2-type major phase was able to retain its ordered structure, as discerned from [Fig. 3(a), (c), and (e)], showing the existence of (100) reflection in Al-10HEA, Al-20HEA, and Al-30HEA having a d-spacing ~ 0.290 nm, respectively. It can be noticed from these figures that the intensity of (202) reflection of the Cr_5Si_3-type phase diminishes after 10 h of MM regardless of the volume fraction of HEA particles in the Al matrix. The asymmetric peak of (202) reflection of Cr_5Si_3-type phase having a d-spacing ~ 0.2069 nm associated with the (110) peak of the B2-type phase of HEA reinforcement was no more evident in the Al-10HEA, Al-20HEA, and Al-30HEA as illustrated in [Fig. 3(b), (d), and (f)], respectively. Further, the (413) reflection of Cr_5Si_3-type phase was also not identified even after 10 h of MM for Al-10HEA, Al-20HEA, and Al-30HEA. It can be inferred from Fig. 3 that no sign of the structural transformation of Al-HEA nanocomposite powder was evident as a function of volume fraction of reinforcement and mechanical milling duration.

Significant broadening and peak shift corresponding to the planes of the Al matrix were evident in Fig. 3. The broadening of peaks corresponding to the Al matrix increased by increasing the volume fraction of HEA particles. The broadening and peak shift of the Al matrix may be correlated with the crystallite size and lattice strain. The variation of crystallite size and lattice strain as a function of milling duration and volume fraction of HEA particles is observed in [Fig. 3(g)–(i)] for Al-10, 20, and 30 HEA, respectively, and reported in Table 2. The volume fraction reinforcement increases the crystallite size refinement and considerably its lattice strain. The crystallite size for Al-10HEA, 20HEA, and 30HEA was found to be ~ 14 nm, 12 nm, and 10 nm, respectively, for the Al matrix MM for 50 h. The lattice strain of these Al matrices was also significant and varied from 0.655 for Al-10HEA to 0.926% for Al-30HEA, as reported in Table 2. This considerable grain refinement and excessive rise in the lattice strain can be attributed to the hard HEA particles consisting of a major B2-type and minor Cr_5Si_3-type phase. It can be observed from [Fig. 3(g)–(i)] that the reduction in crystallite size is very significant up to 30 h of MM. However, after 30 h of MM, the level of crystallite size refinement for Al-10HEA, 20HEA, and 30 HEA was not significant, as indicated in Table 2.

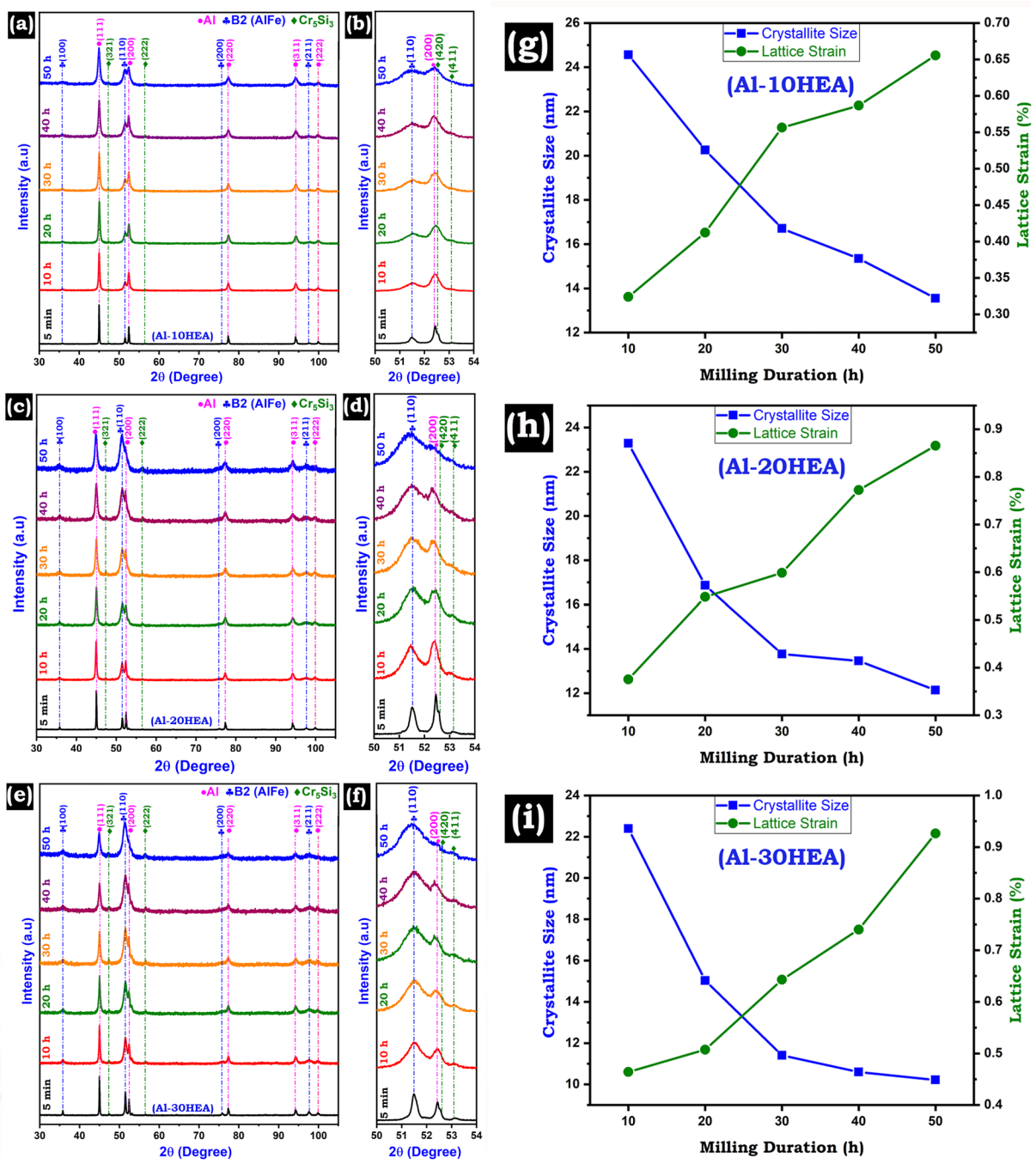

Figure 3: Phase analysis of (a) Al-10HEA nanocomposite powder MM up to 50 h; (b) enlarged image showing co-existence of Al, B2-type, and Cr_5Si_3-type phase in Al-10HEA; (c) Al-20HEA nanocomposite powder MM up to 50 h; (d) enlarged image showing co-existence of Al, B2-type, and Cr_5Si_3-type phase in Al-20HEA; (e) Al-30HEA nanocomposite powder MM up to 50 h; (f) enlarged image showing co-existence of Al, B2-type, and Cr_5Si_3-type phase in Al-30HEA. Variation of crystallite size and lattice strain during mechanical milling of (g) Al-10HEA, (h) Al-20HEA, (i) Al-30HEA.

The diffraction contrast images of Al-30HEA nanocomposite powder milled for 50 h are shown in [Fig. 4(a–c)]. The bright-field (BF) image and corresponding selected area diffraction (SAD) pattern along with the dark field (DF) image are displayed in [Fig. 4(a)–(c)], respectively. Many dark patches corresponding to non-equiatomic HEA particles and strain accumulation are present in the BF image [Fig. 4(a)]. The dark region can be attributed to enhanced grain refinement during severe plastic deformation of the Al matrix in the presence of hard HEA particles. As shown in [Fig. 4(b)],

TABLE 2: Crystallite size, lattice strain, and dislocation density of the Al-HEA nanocomposite powder as a function of milling duration and volume fraction of reinforcement.

Sample designation	Milling duration (h)	Crystallite Size (nm)	Lattice Strain (%)	Dislocation density ρx10^{16} (m^{-2})
Al-10HEA	10	25	0.324	3.6
	20	20	0.412	5.6
	30	17	0.556	9.1
	40	15	0.586	10.4
	50	14	0.655	13.2
Al-20HEA	10	23	0.375	4.4
	20	17	0.548	8.9
	30	14	0.598	11.8
	40	13	0.772	15.7
	50	12	0.865	19.5
Al-30HEA	10	22	0.464	5.7
	20	15	0.507	9.2
	30	11	0.642	15.4
	40	11	0.740	19.1
	50	10	0.926	24.8

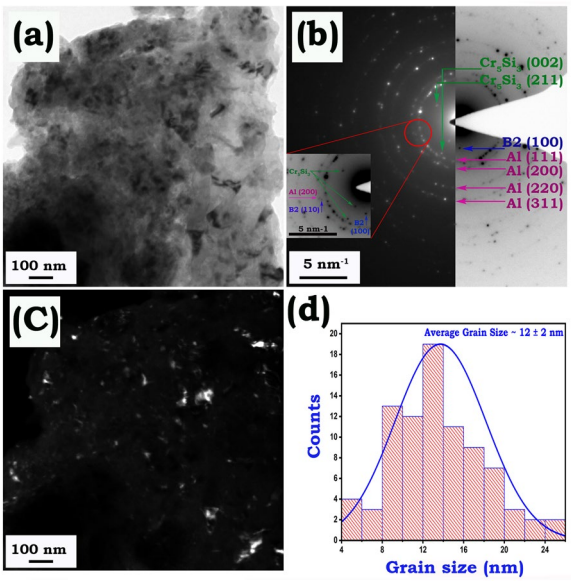

Figure 4: TEM micrograph of Al-30HEA nanocomposite showing the (a) bright-field image (b) corresponding selected area diffraction pattern, (c) dark field image, and (d) grain size distribution in nanocomposites.

the polycrystalline nature of the SAD pattern indicates the random crystallographic texture and nanostructure of the Al matrix in the Al-30HEA nanocomposite powders. The careful observation of the SAD pattern confirms the presence of B2-type and Cr_5Si_3-type phase along with the ring corresponding to the (111) plane of Al. The inset in [Fig. 4(b)] shows the presence of (100) and (110) spots of B2-type phase having a d-spacing ~ 0.290 nm and ~ 0.2056 nm, respectively. The SAD pattern is shown in [Fig. 4(b)] further establishes the presence of (211) and (002) reflection of Cr_5Si_3-type phase having d-spacing ~ 0.3070 nm and 0.2319 nm. B2-type phase in HEA, having interplanar spacing d ~ 0.2056 nm, is very close to that of the (200) reflection of α-Al (d ~ 0.2024 nm). The co-existence of reflection corresponding to the Al matrix and HEA particles was also evident from the powder XRD pattern in Fig. 3. The DF image shows the formation of a nanostructured grain ~ 12 nm by extensive deformation during the repetitive fracturing and cold welding of Al-HEA, as evident from the [Fig. 4(c)] and grain size distribution shown in [Fig. 4(d)]. The size of the nanostructured grains formed after 50 h of MM, observed through TEM may be substantiated by the crystallite size of the Al matrix in the Al-HEA composite, as evident from Table 2. The grain refinement followed through TEM is in line with the XRD results showing the crystallite size ~ 10 nm for Al-30HEA nanocomposite powder milled for 50 h.

The morphology of the AA 6082 Al matrix nanocomposite reinforced with HEA particles is shown in [Fig. 5(a–f)]. It is evident from [Fig. 5(a), (c), and (e)] that for Al-10HEA, 20HEA, and 30HEA that on increasing the volume fraction of HEA particles, the tendency for refinement of the Al matrix increases. The particle size reduction was also discerned from the particle size distribution shown in [Fig. 5(g)–(i)]. The improvement level was maximum for Al-30HEA nanocomposite powder, having a particle size of ~ 1.0 ± 0.2 μm. It is clear from [Fig. 5(a, c, e)] that both the flaky and equiaxed morphology of milled powder after 50 h of MM was observed. The particles with flaky morphology is formed during the initial duration of MM and can be attributed to the extensive deformation of the soft Al matrix in the nanocomposite powder. However, the equiaxed particle morphology was identified when the

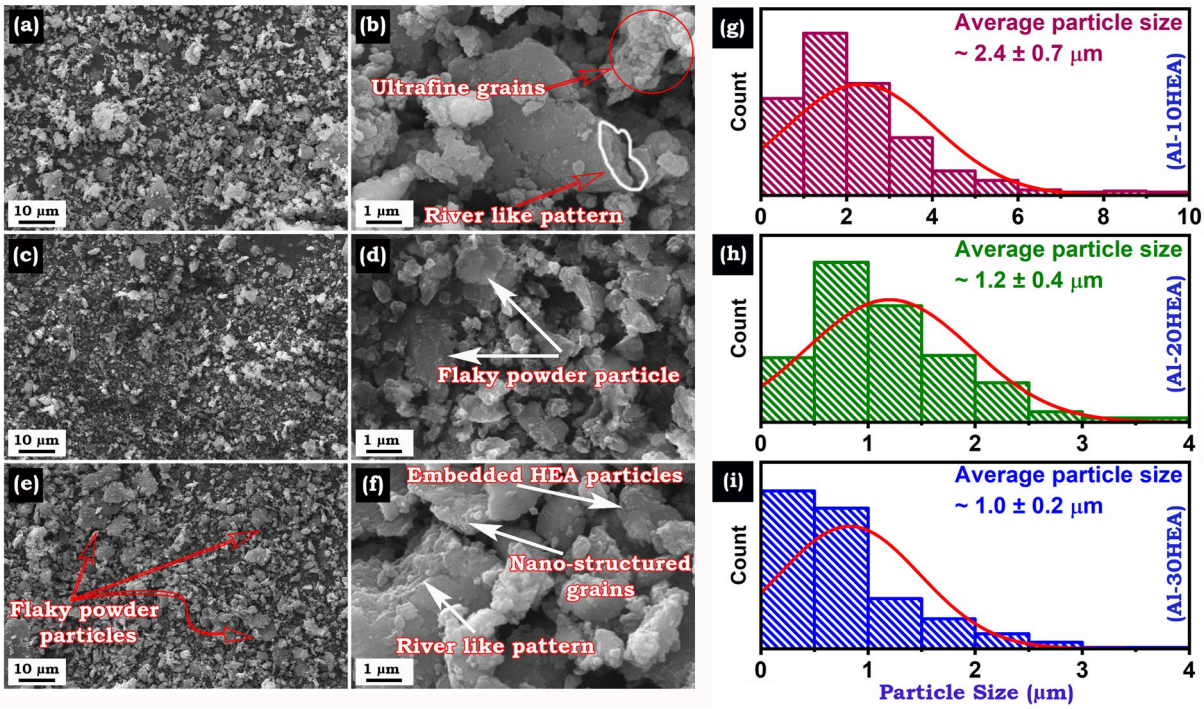

Figure 5: SEM micrograph of Al-HEA nanocomposite powder showing morphology after 50 h of MM in Al-10HEA (a, b), Al-20HEA (c,d), and Al-30HEA at different magnification (e, f). Particle size distribution of (g) Al-10HEA (h) Al-20 HEA and (i) Al-30HEA nanocomposite powder mechanically milled up to 50 h.

MM process reached a steady state. The hard non-equiatomic reinforcement particles further contribute to the fragmentation and nanostructuring of the soft Al matrix. Therefore, after 50 h of milling, the particles are equiaxed, and a few flaky particles were observed in Al-HEA nanocomposite powder.

Further, it can be discerned from [Fig. 5(b), (d), and (f)] for Al-10HEA, 20HEA, and 30HEA that the increase in the volume fraction of HEA particles also enhances the nanostructuring of the ductile Al matrix. Figure 5(b) shows ultrafine grains and river-like patterns. However, increasing the HEA particles in Al-30HEA shown in [Fig. 5(f)] the nanostructured grain was observed, and the thickness of the river like pattern increased. Further, it can be noted that the HEA particles are well embedded in the ductile Al matrix with good interfacial bonding in case of Al-30HEA nanocomposite powder. This can be attributed to the change in milling mechanism due to the increase in hard non-equiatomic HEA particles, enhancing the fragmentation and refinement of the Al matrix during milling.

The thermal stability of the Al-30HEA nanocomposite powder was established through DTA at a scan rate of 20 K/min and in-situ XRD, as shown in [Fig. 6(a) and (b)], respectively. The DTA thermogram of Al-30HEA nanocomposite powders displays the exothermic peaks at T1 until T3, which were found to be negligible as shown in [Fig. 6(a)]. The endothermic peak at T4 can be attributed to the melting of Al matrix in Al-HEA nanocomposite powders. For co-relating the exothermic peaks with any structural transformation, in situ XRD of Al-30HEA nanocomposite powder was carried out at 30 ℃ (300 K), 300 ℃ (573 K), 400 ℃ (673 K), 500 ℃ (773 K), 540 ℃ (813 K), and 560 ℃ (833 K) [Fig. 6(b)]. It can be seen from [Fig. 6(b)] that until 560 ℃ (833 K), no structural transformation of the Al matrix, B2-type, and Cr_5Si_3-type phase in HEA was observed. This confirms the thermal stability of Al-30HEA nanocomposite powder up to 560 ℃ (833 K).

The Al-HEA composite was consolidated by the pressureless sintering method at 560 ℃ (833 K) for 4 h, followed by furnace cooling. For pressure-less sintering, the green compacts of Al-HEA powder were sealed in a quartz tube backfilled with Ar gas. The sintered Al-HEA composite has the same phase observed during the in-situ XRD of nanocomposite powder at 560 ℃ (833 K). The back-scattered electron (BSE) SEM micrograph of Al-10HEA, 20HEA, and 30HEA are shown in [Fig. 7(a, d), (b, e), and (c, f)], respectively. It is observed from [Fig. 7(a)–(c)] that the HEA reinforcement is homogeneously dispersed in the Al matrix. From [Fig. 7(d)–(f)] two distinctively different contrast, namely light gray and dark gray contrast was observed in Al-10HEA, 20HEA, and 30 HEA, respectively. The phases corresponding to these contrast were detected from the elemental analysis of these regions through SEM–EDS techniques.

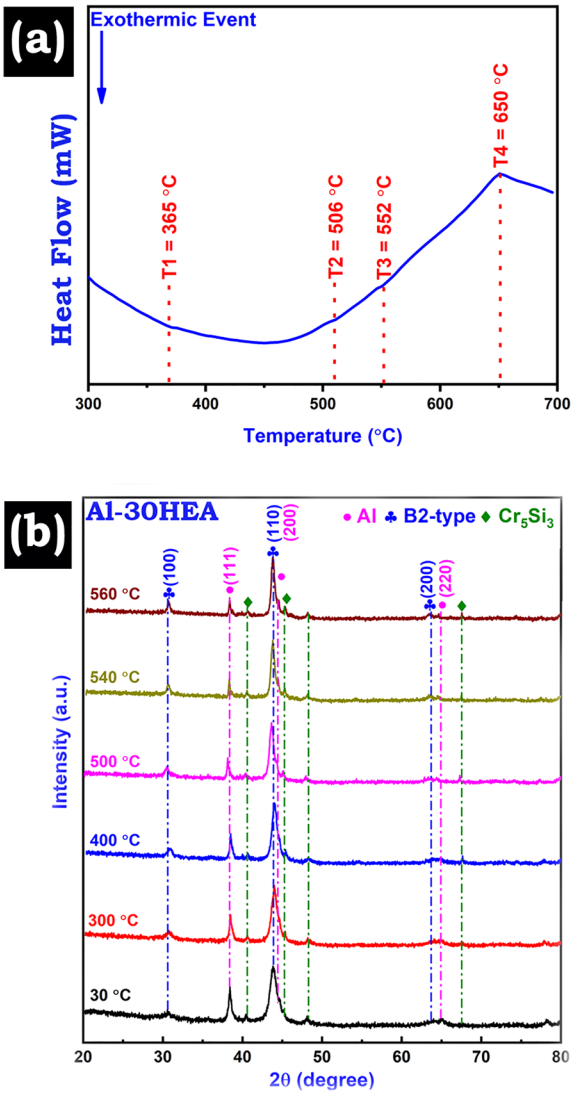

Figure 6: DTA thermogram of (a) Al-30HEA nanocomposite at a 20 K/min scan rate; In situ XRD pattern (λ = 0.15402 nm) of Al-30HEA at high temperatures.

The dark gray contrast has an elemental composition close to that of the Al matrix. However, the light gray contrast has an elemental composition close to that of the non-equiatomic HEA particles. Further, it can be observed that the interfaces in the Al-HEA composite are not sharp; instead were found to be diffused in nature. This interface establishes the good interfacial bonding between Al matrix and HEA reinforcement particles. The diffused nature of interfaces in the Al-30HEA composite was observed through SEM–EDS mapping, as illustrated in [Fig. 7(g)]. The BSE-SEM micrograph depicts the presence of two types of particles, as explained previously. The SEM–EDS mapping discerns the presence of the major B2-type and minor Cr_5Si_3-type phase of HEA particles in the Al matrix. The quasi-spherical particles with a size of ~ 2.0 μm, whose boundary is marked with the white color, was close to the elemental composition of B2-type phase. The intensity of elements like Al, Mn, Fe, Ni, and Cu was found to be high in this region. Apart from this, the small-elongated type of particle whose boundary is marked with black color in the elemental overlay was found to have a high-intensity corresponding to the elements like Cr and Si. The region having a high intensity of Cr and Si also has considerable intensity corresponding to that of Mn. Therefore, it can be inferred that Mn is present in both B2-type and Cr_5Si_3-type phases. Similar to the diffused interfaces seen in [Fig. 7(d)–(f)], a transition layer between the Al matrix and major B2-type phase of HEA was observed in the SEM–EDS mapping demarcated by the orange line seen on the micrograph showing elemental overlay. The thickness of the transitional layer (between the white and orange line) was found to be in the range of ~ 400 to 500 nm [Fig. 7(g)]. Apart from the transition layer, the elements like Fe, Ni, and Cu was found to be present in the Al matrix, as illustrated through the SEM–EDS mapping.

The microhardness of Al-HEA pressure-less sintered composite was evaluated through instrumented indentation techniques. The load versus indentation depth curve for Al-10HEA, 20HEA and 30HEA was shown in [Fig. 7(h)] at a load of 500 mN, to observe the contribution from matrix and reinforcement in the composite. The microhardness and the depth of an indentation are mentioned in Table 3. It can be observed from Table 3 and [Fig. 7(h)] that the microhardness rises considerably (~ 1.81 ± 0.03 GPa) in Al-HEA sintered composite on increasing the volume fraction HEA particles, and the depth of indentation decreases (2.77 ± 0.09 μm). Figures 7(i)–(k) represents the indentation impression on Al-10, 20, and 30HEA pressure-less sintered composite, respectively. On increasing the volume fraction of HEA particles enhances the microhardness of these composites coupled with decrease in the size of indentation impression as evident from the [Fig. 7(i)–(k) and Table 3. The yield strength (YS) of the Al-HEA composite was calculated using Tabor's equation (Yield strength = Hardness/3) [29]. The theoretical YS of the Al-10HEA, 20HEA, and 30HEA was found to be ~ 300 MPa, 504 MPa, and 604 MPa, respectively (Table 3). This high value of microhardness and YS can be attributed to the homogenous distribution of hard non-equiatomic HEA particles and the formation of a transitional layer and solid solution strengthening due to alloying elements in the Al matrix.

Discussion

The present work addresses the exploitation of non-equiatomic AlSiCrMnFeNiCu HEA particles as a reinforcement for designing lightweight, high strength AMCs for structural applications. The non-equiatomic HEA with Al as the principal alloying

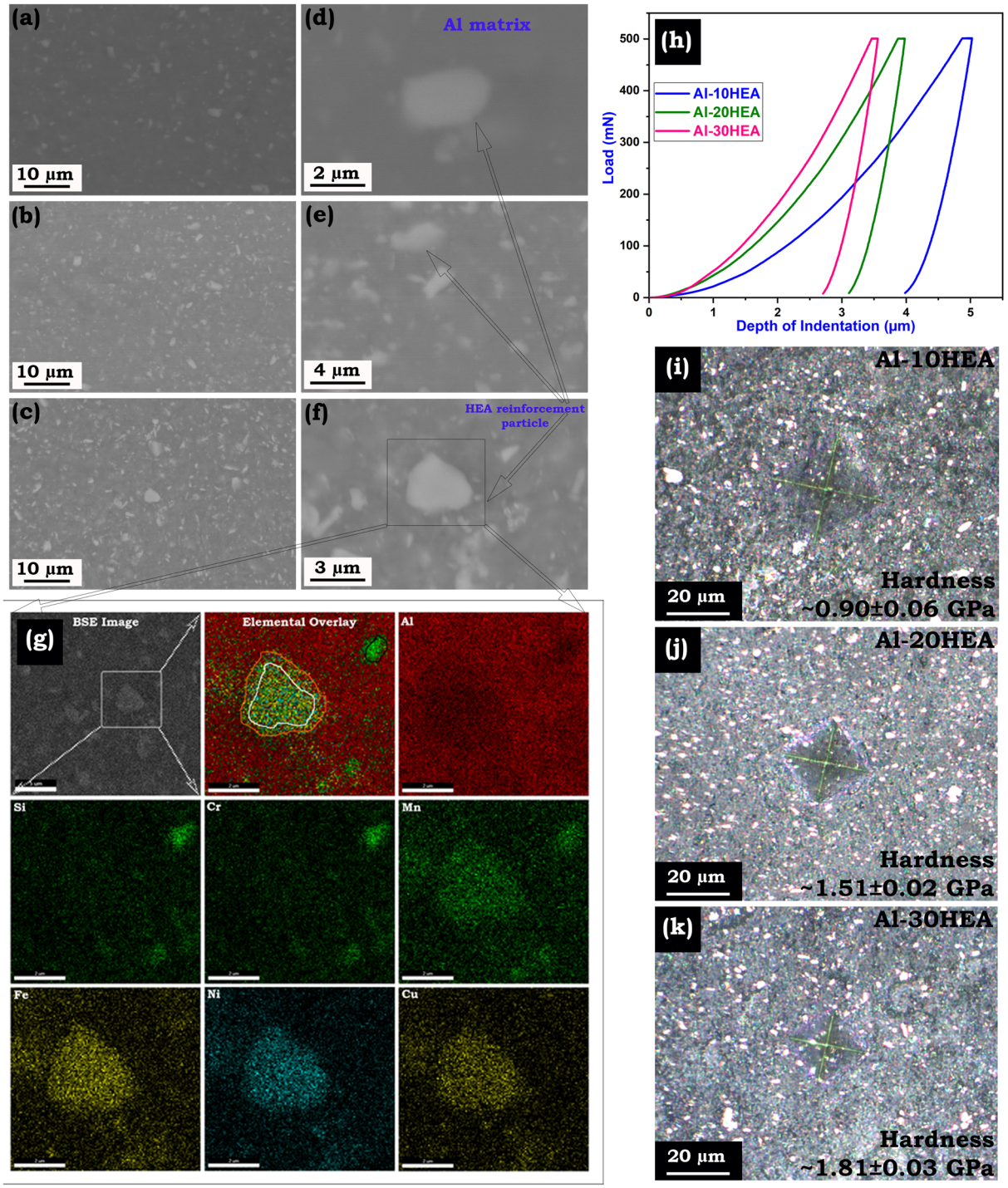

Figure 7: SEM micrograph of (a & d) Al-10HEA, (b & e) Al-20HEA, (c & f) Al-30HEA consolidated by pressure-less sintering at different magnification. (g) SEM–EDS mapping of Al-30HEA composite consolidated by pressure-less sintering showing the formation of transitional layer and elemental distribution. (h) Load versus indentation depth plot for Al-HEA composite. Optical micrograph for the indentation on (i) Al-10HEA (j) Al-20HEA, and (k) Al-30HEA pressure-less sintered composite.

element has shown high hardness and good strength at room temperature and high temperature as well [30–36]. These non-equiatomic HEAs properties can be exploited as reinforcements in AMCs to engineer the desirable interfaces in AMCs.

In the present investigation, a novel attempt has been made to reinforce AMCs with a non-equiatomic AlSiCrMnFeNiCu high-entropy alloy with a low density of ~ 5.08 g.cm^{-3} and high hardness of ~ 7.5 GPa. The concept of non-equiatomic

TABLE 3: Mechanical properties of Al-HEA pressure-less sintered composite.

Sample designation	Hardness (GPa)	Depth of indentation (μm)	Estimated yield strength (MPa)
Al-10HEA	0.90 ± 0.06	4.06 ± 0.14	~ 300
Al-20HEA	1.51 ± 0.02	3.07 ± 0.03	~ 504
Al-30HEA	1.81 ± 0.03	2.77 ± 0.09	~ 604

low-density HEAs are relatively new in contrast to the first report on HEAs by Cantor et al. [37] and Yeh et al. [38]. In the present investigation, efforts were made to prepare new non-equiatomic AlSiCrMnFeNiCu HEAs through VIM. These HEAs were found to have a dual-phase, i.e., B2-type phase and Cr_5Si_3-type phase (Figs. 2, 3). A few researchers have demonstrated the formation of a single B2-type phase in $Al_xCoCrCuFeNi$ ($x \geq 3.0$ mol or 37.5 at.%) [30, 31, 33, 34]. In another investigation, Jin et al. [32] have reported BCC/B2 phase formation along with the minor phase of Cr_3Si for HEA with a nominal composition of $Al_2CoCrFeNiSi$. Similarly, Singh et al. [29, 39, 40] have reported the formation of the minor fraction of the Cr_5Si_3 silicide phase along with the major phases corresponding to BCC and B2-type in MgAlSiCrFe, MgAlSiCrFeNi equiatomic LDHEAs after annealing at above 600 ℃ (873 K).

The MM of Al-HEA leads to its microstructural refinement and increase in the dislocation density (Table 2 and Figs. 3, 4, 5). The microstructural refinement of materials during milling was explained by Suryanarayana [41] and Fetch [42]. During milling, the materials undergo flattening due to collision, cold welding, fracturing, and formation of equiaxed powder particles by random welding followed by steady-state powder particles [42]. In the present investigation, significant microstructural refinement was observed for 30 h milled Al-HEA nanocomposite powders (Fig. 3 and Table 2). During the initial stages of MM, the Al-HEA powder particles entrapped between the colliding WC balls experience a high impact, and the balls' kinetic energy is transferred to them. Therefore, the Al-HEA nanocomposite powder undergoes a high dislocation density leading to its work hardening (Table 2). The dislocation density of the Al-HEA nanocomposite powder was found to increase as a function of volume fraction of reinforcement and duration of MM. However, the crystallite size reduction and increase in the lattice strain and dislocation density are not very significant after 30 h of MM (Fig. 3 and Table 2). During prolonged duration of MM, the rate of plastic deformation usually reduces the extent of an increase in the dislocation density, as evident from Table 2. Therefore, the crystallite size refinement and increase in the lattice strain after 30 h of milling Al-HEA nanocomposite powder were not very appreciable.

Fetch [42] has explained that the formation of steady-state powder particles is usually responsible for saturation in the refinement of grains and powder particles during milling. Similar observations were also made by Basariya et al. [43] and Shadangi et al. [44] for 6082 Al matrix composites. Further, Shadangi et al. [44] have shown that the Al–Cu–Fe icosahedral quasicrystalline (IQC) particles were well embedded inside the Al matrix during milling up to 50 h. However, in the present investigation, structural transformation or interfacial reaction was not evident in Al-HEA nanocomposites milled upto 50 h, contrary to the observation of Shadangi et al. [44] during MM of Al-IQC. A few researchers and co-workers have suggested the structural transformation of periodic and aperiodic intermetallics are usually due to the ballistic jump of atoms [45–49]. In the present investigation, the mechanism of MM is mostly ductile–brittle type due to the presence of soft FCC-Al and hard HEA reinforcement. These HEA particles could retain their ordering even after prolonged milling for 50 h (Figs. 3, 4). In our previous investigation, attempts were made to synthesize low-density HEAs through mechanical alloying [29, 39, 40, 50]. It was observed that the LDHEAs containing Mg invariably undergo structural transformation above ~ 400 ℃ (673 K) regardless of alloying elements. However, in the present work, the HEAs reinforced in AMCs retained their identity until melting of Al-matrix (Fig. 6). In a recent work on the laser ablation of these non-equiatmic AlSiCrFeMnNiCu HEAs, Rawat et al. [51] have shown the phase stability of laser ablated nanoparticles of B2-type and Cr_5Si_3 phases along with Cu-Ni enriched regions. Therefore, these non-equiatomic HEAs ought to have good stability up to the melting temperature of Al-matrix.

The thermal analysis of nanocomposite powder was conducted to investigate any possible interfacial reactions in Al-HEA composite. The minor exothermic fluctuations were observed in the DTA thermogram, as evident from [Fig. 6(a)]. However, the in situ XRD confirmed no structural transformation of either the primary B2-type phase or the minor Cr_5Si_3 type phase in non-equiatomic HEA in Al-HEA composite samples. The Al matrix was also found to retain its identity until 560 ℃ (833 K). The small exothermic fluctuations can be corroborated with the strain relaxation and dissolution of the minor amount of alloying elements from the non-equiatomic HEA into the Al matrix. Similar observations were made by Basaria et al. [43, 52] for Al–Mg–Si-based alloy reinforced with garnet and CNTs. They have shown the minor exothermic fluctuations due to the dissolution of Mg and Si in the Al matrix during the heating of nanocomposite powder in DTA up to 700 ℃ (973 K). The dissolution of alloying elements at higher temperatures can be attributed to the physical parameter like the self-diffusion coefficient (Table 1). The chances for dissolution of alloying elements with low self-diffusion co-efficient is almost negligible. The elements with higher values of the self-diffusion coefficient

and thermal conductivity are more prone to dissolve in the Al matrix (Table 1).

As illustrated in Table 3, the Al-HEA composite consolidated by pressure-less sintering was found to have appreciable microhardness and yield strength. However, no signature pertaining to structural transformation was evident from in situ XRD results or the SEM micrographs of Al-HEA composite shown in [Figs. 6(b) and 7], respectively. However, the diffused nature of interfaces was quite prevalent in the Al matrix reinforced with non-equiatomic HEA. The careful examination of the diffused interfaces indicates the presence of a transitional layer [Fig. 7(g)]. Therefore, the enhanced mechanical properties can be attributed to the formation of a transitional layer having thickness in the range of ~ 400–500 nm and the HEA particles' homogenous distribution in the Al matrix. A few investigators have reported the formation of the transition layer and homogenous distribution of reinforcement responsible for enhanced mechanical properties.

In a study, Liu et al. [17] observed the formation of a transition layer between the Al matrix and AlCoCrFeNi HEA particles. They have discerned the progressive increase in the thickness of the transition layer as a function of SPS temperature varied from 540 to 600 ℃. The increase in the transition layer thickness enhances the strength of AMCs reinforced with 5 vol% of AlCoCrFeNi HEA particles. They have observed the gradient in the hardness gradually decreasing with increasing the transition layer thickness. This may be attributed to the change FCC crystal structure in the transition layers arising from interfacial reaction between Al matrix and HEA reinforcement having BCC structure. They have suggested the increase in strength may be due to the change in stress conditions to iso-strain from iso-stress. The YS of these composites were found to increase as a function of heat treatement temperatures. These AMCs heat treated at 540 ℃, 560 ℃, and 580 ℃ were found to have a YS of ~ 96 MPa, ~ 105 MPa, and 137 MPa, respectively. Yuan et al. [23] observed the microstructure and properties of 2024 Al alloy reinforced with CoCrFeMnNi HEA (known as Cantor alloy). They have demonstrated the transition layer formation due to interfacial reaction between Cantor alloys and 2024 Al alloys. The thickness of the transition layer of ~ 6 μm, separated into two parts, i.e., the inner diffusion layer and outer diffusion layer, with different elemental distribution due to the variation of the diffusion coefficient and modes of the alloying elements in Cantor alloy. The formation of gradient transition layers enhances the hardness of AMCs to 135 HV from 80 HV with 7 vol% of HEA reinforcement. The findings of Yuan et al. [23] are very close to the present results for Al-10HEA fabricated by pressure-less sintering. The slight deviation in the results can be attributed to the sintering method incorporated. In another investigation, Lu et al. [16] have reported the formation of transitional layer between 6061 Al matrix reinforced with 7.5 vol% of $CoNiFeAl_{0.4}Ti_{0.6}Cr_{0.5}$ HEA reinforcement through ball milling followed by hot-pressing (at 490 ℃, 120 MPa) and hot extrusion (at 450 ℃ with 10:1 extrusion ratio). These AMCs were solution strengthened at 510 ℃ (783 K) followed by aging at 175 ℃ for 5 h. The YS and ultimate strength of the AMCs prepared by Lu et al. [16] was found to ~ 348 MPa and ~ 385 MPa, respectively. The tremendous enhancement in the mechanical properties may be attributed to the formation of θ-Al_2Cu phase at the interface of Al matrix and HEA reinforcement.

Apart from forming a transition layer between Al and HEA particles, the solid solution strengthening can also be attributed to Al-HEA composites' enhanced mechanical properties fabricated by a cost-effective pressure-less sintering method in the present investigation. The SEM–EDS mapping shows elements like Cu, Fe, and Ni in the Al matrix. The intensity of Cu in the Al matrix was very prominent compared to Fe and Ni. This can be attributed to Cu's high self-diffusion coefficient and thermal conductivity (Table 1). Another essential observation was made by Wang et al. [36] regarding the formation of a transition layer during the SPS of pure Al matrix and CuZrNiAlTiW HEA particles having a single BCC phase. Due to the interfacial reaction, the interfacial layer induces the hybridization of AMCs by forming B2-NiAl type and WAl_{12} type phases in the transitional layer. The in situ formation of B2-NiAl type and WAl_{12} type phases enhances the microhardness of AMCs reinforced with 30 vol% of CuZrNiAlTiW HEA particles and is approximately ten times more than that of the pure Al. They have reported enhanced ultimate strength ~ 544 MPa with appreciable ductility of ~ 7.0% for AMCs with 20 vol% of HEA reinforcement. However, on increasing the volume fraction of HEA reinforcement in the AMCs, the ultimate strength was found to be ~ 270 MPa with elongation of ~ 3.0%. Although the strength was more than the unreinforced samples, however reduction in strength was observed w.r.t to AMCs with 20 vol% of HEA reinforcement. Similarly, the formation of core–shell structure in the AMCs reinforced with 10 vol% of HEA demonstrates good compressive strength. The excellent mechanical properties of the AMCs can be attributed to the precipitation hardening and dispersion strengthening due to the formation of B2-NiAl type and WAl_{12} type phases and uniform distribution of HEA particles having BCC phase, respectively.

Yuan et al. [53] have attempted to fabricate 7.0 vol% of $Al_{0.6}CoCrFeNi$ HEA reinforced AMCs by hot pressing followed by heat treatment at 350 ℃, 500 ℃, and 600 ℃ for 24 h. They have observed no distinct transition at the interface of 5052 Al alloy matrix. However, during heat treatment above 500 ℃, they have identified the formation of the core–shell structure previously reported by Wang et al. [54]. They have established that the thickness of the interfacial layer depends on the heat treatment

temperature and the duration of heat treatment [53]. The formation of interfacial layer led significant improvement in the mechanical properties. The AMCs heat treated at 500 ℃ (773 K) for 24 h and 48 h show high hardness of ~ 1.81 GPa and ~ 1.61 GPa, respectively.

The high-temperature stability of a major B2-type HEA has led to the synthesis of Al-HEA composite having a transitional layer with a thickness in the range of ~ 400–500 nm between the Al matrix and the HEA reinforcement leading to the enhancement of the microhardness and the yield strength of the composite. The Al-HEA composite interfaces can be engineered to form the transition layer between the Al matrix and HEA particles. This type of interface will inhibit the formation of cracks at the interfaces of matrix and reinforcement, on contrary to MMCs reinforced with ceramic particulates. This strategy will help designing lightweight AMCs suitable for the automotive sector.

Conclusion

The mechanical milling of 6082 Al matrix reinforced with the varying volume fraction of non-equiatomic AlSiCrMnFeNiCu HEA particles up to 50 h of MM, and its consolidation by cost-effective pressure-less sintering significantly enhances its grain refinement and microhardness. The following can be concluded from the present investigation:

1. A new non-equiatomic AlSiCrMnFeNiCu high-entropy alloy having a primary B2-type phase coexisting with a minor amount of Cr_5Si_3-type phase synthesized by vacuum induction melting was used as a reinforcement for Al matrix nanocomposites.
2. The non-equiatomic HEA particles in the Al-HEA nanocomposite powder retain their structural characteristics even after 50 h of milling. Increasing the volume fraction of non-equiatomic HEA particles in Al-HEA nanocomposite powder enhances its nanostructuring with minimum grain size of ~ 10–12 nm.
3. The Al-HEA nanocomposite powder was found to be thermally stable up to 650 ℃ (923 K) until the melting of Al matrix.
4. The pressureless sintering of the Al-HEA composite led to formation of diffused interfaces between the matrix and the HEA reinforcement particles. A transitional layer having a thickness in the range of ~ 400–500 nm was formed at the diffused interfaces in the Al-HEA composite.
5. The formation of a transition layer between the non-equiatomic HEA particles and the Al matrix enhances the microhardness and yield strength of Al-30HEA ~ 1.81 GPa and 604 MPa, respectively. The increase in these composites microhardness may be attributed to direct and indirect strengthening effects arising from HEA particles.

Experimental details

The metallic shots of Al, Si, Cr, Mn, Fe, Ni, and Cu (purity ≥ 99%; Alfa Aesar India Pvt. Ltd.) were used to synthesize non-equiatomic AlSiCrMnFeNiCu HEA. The non-equiatomic $Al_{40}(SiCrMnFeNiCu)_{60}$ (at.%) HEA was prepared using vacuum induction melting. The as-cast HEA was prepared by taking individual metal of Al, Si, Cr, Mn, Fe, Ni & Cu (in non–equiatomic proportion) weighing 1 kg was placed in an alumina crucible inside the chamber of vacuum induction melting. The alumina crucible containing the metal shots were surrounded by water-cooled copper coils for supplying AC current connected to solid-state RF generator. The chamber was backfilled with argon gas to avoid the evaporation of metals due to the difference in the melting point of constituent elements. After melting and homogenous mixing of metallic elements in the alumina crucible, the molten alloy was poured into the water-cooled copper crucible. During the VIM, the temperature of molten metal was monitored with the help of an optical pyrometer. The HEA was poured at a temperature of ~ 1400 ℃ (1673 K) [as shown in [Fig. 1(a)]. The as-cast non-equiatomic HEA had a density of 5.08 g cm^{-3} and was calculated as per the procedure described elsewhere [55].

Vibratory ball milling (KC-0, Tau Instruments) was used for crushing and fragmenting the as-cast non–equiatomic AlSiCrMnFeNiCu HEA into powder particles with a size of ≤ 10 μm for 30 min using a ball to powder ratio (BPR) of 100:1. These powder particles were used to synthesize Al-HEA nanocomposite powders through high energy ball milling. The details of the age-hardenable AA 6082 Al alloy powders used in the present investigation are mentioned in our previous study [43, 44]. The AA 6082 Al matrix was reinforced with 10, 20, and 30 volume fractions of AlSiCrMnFeNiCu HEA. The matrix and reinforcement particles were pre-mixed in the desired proportion as mentioned in Table S1. These pre-mixed powders of Al-HEA were mechanically milled (MM) up to 50 h in a high energy planetary ball mill (PM 400, Retsch, Germany) using toluene as process control reagent in order to avoid oxidation during milling. The milled samples were withdrawn after every 10 h of MM. The milling was intermittently stopped for 15 min after every 30 min of milling to avoid any rise in the temperature. The details of process parameters are mentioned in our previous investigation [27]. The green pellets (diameter of 12 mm) of these Al-HEA nanocomposite powders were prepared by cold pressing at a load of 5 Ton. These green pellets were vacuum-sealed in a quartz tube and back purged with argon [27] to avoid any possibility of oxidation during pressure-less sintering. These Al-HEA pellets were consolidated through pressure-less sintering at 560 ℃ (833 K) for 4 h, followed by furnace cooling. The schematic for preparation of Al-HEA nanocomposite powders and its

consolidation through pressure-less sintering is shown in the [Fig. 1(b) and (c)], respectively.

The phase analysis of these nanocomposite powders was ascertained through XRD (EMPYREAN, PANALYTICAL). A CoKα source ($\lambda = 0.17909$ nm) with a scanning speed of 10° min^{-1} was used at an operating voltage and current of 40 kV and 40 mA, respectively, for XRD analysis. The fine microstructural features of these Al-HEA nanocomposite powders were observed through TEM (TECNAI G^2 T20, FEI) in diffraction contrast mode at an operating voltage of 200 kV. The morphology and chemical composition of nanocomposite powders were discerned through SEM–EDS investigation. The thermal stability of the 50 h milled Al-30HEA nanocomposite powders were examined to study the phase evolution using differential thermal analysis (DTA) (DSC 404 F3, Pegasus, Netzsch, Germany) under nitrogen atmosphere with a heating rate of 20 K/min. The phase evolution during DTA was co-related with phases formed in the Al-30HEA nanocomposite powder at 30 °C, 300 °C, 400 °C, 500 °C, 540 °C, and 560 °C observed through in-situ XRD (SmartLab, 9 kW, Rigaku) which was done with a Cu-Kα source ($\lambda = 0.15402$ nm) with a scanning speed of 5° min^{-1}.

The microstructure and elemental distribution in Al-HEA pressure-less sintered composites were investigated through SEM and SEM–EDS mapping. Further, the microhardness of these sintered composites was evaluated through instrumented indentation tester (MHT^3, Anton Paar) at a load of 500 mN with a loading/unloading rate of 1000 mN min^{-1}, and dwell time of 20 s. The optical micrograph corresponding to the indents were captured with the help of optical microscope retrofitted with the instrumented indentation tester. At least ten (10) readings were taken to calculate average microhardness and corresponding standard deviation. The hardness of these composites were computed through Oliver–Pharr method [29]. The samples for instrumented indentation were prepared by hot mounting the pressure-less sintered samples in epoxy. These hot-mounted samples were polished using standard metallographic techniques for indentation. The Tabor's law mentioned in Eq. (1) is used for calculating the theoretical yield strength (YS) as described as below:

$$Theoretical\ Yield\ Strength(YS) = \frac{Hardness}{3} \quad (1)$$

Acknowledgments

The authors would like to thank Profs. S Lele, R K Mandal, and Drs. Joysurya Basu and Vikas Shivam for many stimulating discussion. Authors will also like to acknowledge Dr Rampada Manna's support for extending the characterization facility of ARCIS and Dr Bhaskar Majumdar for vacuum induction melting. The Central Instrument Facility, IIT (BHU) for extending the necessary characterisation facility is thankfully acknowledged. The authors will also like to acknowledge DST-FIST (Level-II) for infrastructural support. The authors gratefully acknowledge the support and help of Mr. Lalit Kumar Singh and Mr. Girish Sahoo for TEM and SEM investigation, respectively. YS recognizes the support of BK21 postdoctoral researchers at Seoul National University and global postdoctoral researchers. YS would like to acknowledge assistance of Mr. Harsh Jain, Mr. Priyatosh Pradhan and Mr. G Suryaprakash Goud during experimentation.

Data availability

Data will be made available on reasonable request.

Declarations

Conflict of interest On behalf of all authors, the corresponding author states that there is no conflict of interest.

Open Access

Supplementary Information

The online version contains supplementary material available at https://doi.org/10.1557/s43578-022-00866-x.

References

1. K.K. Chawla, N. Chawla, *Metal Matrix Composites* (Springer, New York, 2006)
2. F. Tang, I.E. Anderson, S.B. Biner, Microstructures and mechanical properties of pure Al matrix composites reinforced by Al-Cu-Fe alloy particles. Mater. Sci. Eng. A **363**, 20–29 (2003). https://doi.org/10.1016/S0921-5093(03)00433-7
3. F. Tang, H. Meeks, J.E. Spowart, T. Gnaeupel-Herold, H. Prask, I.E. Anderson, Consolidation effects on tensile properties of an

elemental Al matrix composite. Mater. Sci. Eng. A **386**, 194–204 (2004). https://doi.org/10.1016/j.msea.2004.07.040

4. G. Britain, P. Press, M. Science, E.T.S. Ingenieros, An analysis of the effects of matrix void metal-ceramic composites. Acta Met. Mater. **39**, 2317–2335 (1991)
5. F. Tang, I.E. Anderson, T. Gnaupel-Herold, H. Prask, Pure Al matrix composites produced by vacuum hot pressing: tensile properties and strengthening mechanisms. Mater. Sci. Eng. A **383**, 362–373 (2004). https://doi.org/10.1016/j.msea.2004.05.081
6. Y. Xie, X. Meng, Y. Chang, D. Mao, Y. Yang, Y. Xu, L. Wan, Y. Huang, Ameliorating strength-ductility efficiency of graphene nanoplatelet-reinforced aluminum composites via deformation-driven metallurgy. Compos. Sci. Technol. **219**, 109225 (2022). https://doi.org/10.1016/j.compscitech.2021.109225
7. Y. Xie, X. Meng, Y. Chang, D. Mao, Z. Qin, L. Wan, Y. Huang, Heteroatom modification enhances corrosion durability in high-mechanical-performance graphene-reinforced aluminum matrix composites. Adv. Sci. **9**, 2104464 (2022). https://doi.org/10.1002/advs.202104464
8. R.N. Shahid, S. Scudino, Microstructural strengthening by phase transformation in Al-Fe_3Al composites. J. Alloys Compd. **705**, 590–597 (2017). https://doi.org/10.1016/j.jallcom.2017.02.157
9. B.S. Murty, J.W. Yeh, S. Ranganathan, High-Entropy Alloys, 1st ed., BUTTERWORTH HEINEMANN, 2014.
10. D.B. Miracle, O.N. Senkov, A critical review of high entropy alloys and related concepts. Acta Mater. **122**, 448–511 (2017). https://doi.org/10.1016/j.actamat.2016.08.081
11. Z.W. Wang, Y.B. Yuan, R.X. Zheng, K. Ameyama, C.L. Ma, Microstructures and mechanical properties of extruded 2024 aluminum alloy reinforced by $FeNiCrCoAl_3$ particles. Trans. Nonferr. Met. Soc. China **24**, 2366–2373 (2014). https://doi.org/10.1016/S1003-6326(14)63358-6
12. J. Chen, P. Niu, T. Wei, L. Hao, Y. Liu, X. Wang, Y. Peng, Fabrication and mechanical properties of AlCoNiCrFe high-entropy alloy particle reinforced Cu matrix composites. J. Alloys Compd. **649**, 630–634 (2015). https://doi.org/10.1016/j.jallcom.2015.07.125
13. Q. Zhang, H. Xu, X.H. Tan, X.L. Hou, S.W. Wu, G.S. Tan, L.Y. Yu, The effects of phase constitution on magnetic and mechanical properties of FeCoNi(CuAl) x (x = 0–1.2) high-entropy alloys. J. Alloys Compd. **693**, 1061–1067 (2017). https://doi.org/10.1016/j.jallcom.2016.09.271
14. G.M. Karthik, S. Panikar, G.D.J. Ram, R.S. Kottada, Additive manufacturing of an aluminum matrix composite reinforced with nanocrystalline high-entropy alloy particles. Mater. Sci. Eng. A **679**, 193–203 (2017). https://doi.org/10.1016/j.msea.2016.10.038
15. T. Lu, S. Scudino, W. Chen, P. Wang, D. Li, M. Mao, L. Kang, A particles addition on microstructure and mechanical properties of SiC p/7075Al composites. Mater. Sci. Eng. A **726**, 126–136 (2018). https://doi.org/10.1016/j.msea.2018.04.080
16. W. Chen, Z. Li, T. Lu, T. He, R. Li, B. Li, B. Wan, Z. Fu, S. Scudino, Effect of ball milling on microstructure and mechanical properties of 6061Al matrix composites reinforced with high-entropy alloy particles. Mater. Sci. Eng. A **762**, 138116 (2019). https://doi.org/10.1016/j.msea.2019.138116
17. Y. Liu, J. Chen, Z. Li, X. Wang, X. Fan, J. Liu, Formation of transition layer and its effect on mechanical properties of AlCoCrFeNi high-entropy alloy/Al composites. J. Alloys Compd. **780**, 558–564 (2019). https://doi.org/10.1016/j.jallcom.2018.11.364
18. T. Lu, W. Chen, Z. Li, T. He, B. Li, R. Li, Z. Fu, S. Scudino, Processing and mechanical properties of fine grained Al matrix composites reinforced with a uniform dispersion of nanocrystalline high-entropy alloy particles. J. Alloys Compd. **801**, 473–477 (2019). https://doi.org/10.1016/j.jallcom.2019.06.157
19. K.S. Tun, M. Gupta, Enhanced mechanical properties and near unity yield asymmetry in equiatomic high entropy alloy particles reinforced magnesium composites. J. Alloys Compd. **810**, 151909 (2019). https://doi.org/10.1016/j.jallcom.2019.151909
20. H.Y. Yu, F.A. Wei, R.B. Chang, P.G. Ji, Q.Z. Wang, Modifying element diffusion pathway by transition layer structure in high-entropy alloy particle reinforced Cu matrix composites. Trans. Nonferr. Met. Soc. China **29**, 2331–2339 (2019). https://doi.org/10.1016/S1003-6326(19)65139-3
21. X. Yang, P. Dong, Z. Yan, B. Cheng, X. Zhai, H. Chen, H. Zhang, W. Wang, AlCoCrFeNi high-entropy alloy particle reinforced 5083Al matrix composites with fine grain structure fabricated by submerged friction stir processing. J. Alloys Compd. **836**, 155411 (2020). https://doi.org/10.1016/j.jallcom.2020.155411
22. Z. Tan, L. Wang, Y. Xue, P. Zhang, T. Cao, X. Cheng, High-entropy alloy particle reinforced Al-based amorphous alloy composite with ultrahigh strength prepared by spark plasma sintering. Mater. Des. **109**, 219–226 (2016). https://doi.org/10.1016/j.matdes.2016.07.086
23. Z. Yuan, W. Tian, F. Li, Q. Fu, Y. Hu, X. Wang, Microstructure and properties of high-entropy alloy reinforced aluminum matrix composites by spark plasma sintering. J. Alloys Compd. **806**, 901–908 (2019). https://doi.org/10.1016/j.jallcom.2019.07.185
24. X. Yang, X. Zhai, P. Dong, Z. Yan, B. Cheng, H. Zhang, W. Wang, Interface characteristics of high-entropy alloy/Al-Mg composites by underwater friction stir processing. Mater. Lett. **275**, 128200 (2020). https://doi.org/10.1016/j.matlet.2020.128200
25. K. Praveen Kumar, M. Gopi Krishna, J. Babu Rao, N.R.M.R. Bhargava, Fabrication and characterization of 2024 aluminium—high entropy alloy composites. J. Alloys Compd. **640**, 421–427 (2015). https://doi.org/10.1016/j.jallcom.2015.03.093
26. Y. Zhang, X. Li, H. Gu, R. Li, P. Chen, C. Kong, H. Yu, Insight of high-entropy alloy particles-reinforced 2219 Al matrix composites

via the ultrasonic casting technology. Mater. Charact. **182**, 111548 (2021). https://doi.org/10.1016/j.matchar.2021.111548

27. K. Soorya Prakash, P.M. Gopal, M. Purusothaman, M. Sasikumar, Fabrication and characterization of metal-high entropy alloy composites. Int. J. Met. **14**, 547–555 (2020). https://doi.org/10.1007/s40962-019-00383-4
28. J. Li, Y. Li, F. Wang, X. Meng, L. Wan, Z. Dong, Y. Huang, Friction stir processing of high-entropy alloy reinforced aluminum matrix composites for mechanical properties enhancement. Mater. Sci. Eng. A **792**, 139755 (2020). https://doi.org/10.1016/j.msea.2020.139755
29. N. Singh, Y. Shadangi, V. Shivam, N.K. Mukhopadhyay, MgAlSiCrFeNi low-density high entropy alloy processed by mechanical alloying and spark plasma sintering: effect on phase evolution and thermal stability. J. Alloys Compd. **875**, 159923 (2021). https://doi.org/10.1016/j.jallcom.2021.159923
30. C.J. Tong, M.R. Chen, S.K. Chen, J.W. Yeh, T.T. Shun, S.J. Lin, S.Y. Chang, Mechanical performance of the AlxCoCrCuFeNi high-entropy alloy system with multiprincipal elements. Metall. Mater. Trans. A **36**, 1263–1271 (2005). https://doi.org/10.1007/s11661-005-0218-9
31. H. Ziaei, B. Sadeghi, Z. Marfavi, N. Ebrahimzadeh, P. Cavaliere, Phase evolution in mechanical alloying and spark plasma sintering of AlxCoCrCuFeNi HEAs. Mater. Sci. Technol. **36**, 604–614 (2020). https://doi.org/10.1080/02670836.2020.1722912
32. B. Jin, N. Zhang, H. Yu, D. Hao, Y. Ma, AlxCoCrFeNiSi high entropy alloy coatings with microhardness and impreoved wear resistance. Surf. Coat. Technol. **402**, 126328 (2020)
33. R. Sriharitha, B.S. Murty, R.S. Kottada, Alloying, thermal stability and strengthening in spark plasma sintered AlxCoCrCuFeNi high entropy alloys. J. Alloys Compd. **583**, 419–426 (2014)
34. R. Sriharitha, B.S. Murty, R.S. Kottada, Phase formation in mechically alloyed AlxCoCrCuFeNi (x=0.45, 1, 2.5, 5 mol) high entropy alloys. Intermetallics **32**, 119–126 (2013)
35. W.R. Wang, W.L. Wang, S.C. Wang, Y.C. Tsai, C.H. Lai, J.W. Yeh, Effects of Al addition on the microstructure and mechanical property of Al xCoCrFeNi high-entropy alloys. Intermetallics **26**, 44–51 (2012). https://doi.org/10.1016/j.intermet.2012.03.005
36. Y. Zhou, Y. Zhang, Y. Wang, G. Chen, Microstructure characterization of Alx(TiVCrMnFeCoNiCu)100–x high-entropy alloy system with multi-principal elements. Xiyou Jinshu Cailiao Yu Gongcheng/Rare Met. Mater. Eng. **36**, 2136–2139 (2007)
37. B. Cantor, I.T.H. Chang, P. Knight, A.J.B. Vincent, Microstructural development in equiatomic multicomponent alloys. Mater. Sci. Eng. A **375–377**, 213–218 (2004). https://doi.org/10.1016/j.msea.2003.10.257
38. J.W. Yeh, S.K. Chen, S.J. Lin, J.Y. Gan, T.S. Chin, T.T. Shun, C.H. Tsau, S.Y. Chang, Nanostructured high-entropy alloys with multiple principal elements: novel alloy design concepts and outcomes. Adv. Eng. Mater. **6**, 299–303 (2004). https://doi.org/10.1002/adem.200300567
39. N. Singh, Y. Shadangi, N.K. Mukhopadhyay, Phase evolution and thermal stability of low-density MgAlSiCrFe high-entropy alloy processed through mechanical alloying. Trans. Indian Inst. Met. (2020). https://doi.org/10.1007/s12666-020-02039-y
40. N. Singh, Y. Shadangi, G.S. Goud, V.K. Pandey, V. Shivam, N.K. Mukhopadhyay, Fabrication of MgAlSiCrFe low-density high-entropy alloy by mechanical alloying and spark plasma sintering. Trans. Indian Inst. Met. **74**, 2203–2219 (2021). https://doi.org/10.1007/s12666-021-02262-1
41. C. Suryanarayana, Mechanical alloying and milling. Prog. Mater. Sci. **46**, 1–184 (2001). https://doi.org/10.1016/S0079-6425(99)00010-9
42. H.J. Fetch, Nanostructure formation by mechanical attirition. Nanostruct. Mater. **6**, 33–42 (1995)
43. M. Raviathul Basariya, V.C. Srivastava, N.K. Mukhopadhyay, Effect of milling time on structural evolution and mechanical properties of garnet reinforced EN AW6082 composites. Metall. Mater. Trans. A **46**, 1360–1373 (2014). https://doi.org/10.1007/s11661-014-2685-3
44. Y. Shadangi, S. Sharma, V. Shivam, J. Basu, K. Chattopadhyay, B. Majumdar, N.K. Mukhopadhyay, Fabrication of Al–Cu–Fe quasicrystal reinforced 6082 aluminium matrix nanocomposites through mechanical milling and spark plasma sintering. J. Alloys Compd. **828**, 154258 (2020). https://doi.org/10.1016/J.JALLCOM.2020.154258
45. N.K. Mukhopadhyay, F. Ali, V.C. Srivastava, T.P. Yadav, M. Sakaliyska, K.B. Surreddi, S. Scudino, V. Uhlenwinkel, J. Eckert, Strain-induced structural transformation of single-phase Al–Cu–Fe icosahedral quasicrystal during mechanical milling. Philos. Mag. **91**, 2482–2490 (2011). https://doi.org/10.1080/14786435.2010.536178
46. M.R. Basariya, R.K. Roy, A.K. Pramanick, V.C. Srivastava, N.K. Mukhopadhyay, Structural transition and softening in Al-Fe intermetallic compounds induced by high energy ball milling. Mater. Sci. Eng. A **638**, 282–288 (2015). https://doi.org/10.1016/j.msea.2015.04.076
47. M.R. Basariya, V.C. Srivastava, N.K. Mukhopadhyay, Inverse Hall—Petch like behaviour in a mechanically milled nanocrystalline Al 5 Fe 2 intermetallic phase. Philos. Mag. **6435**, 1–12 (2016). https://doi.org/10.1080/14786435.2016.1204474
48. Y. Shadangi, V. Shivam, M.K. Singh, K. Chattopadhyay, J. Basu, N.K. Mukhopadhyay, Synthesis and characterization of Sn reinforced Al-Cu-Fe quasicrystalline matrix nanocomposite by mechanical milling. J. Alloys Compd. **797**, 1280–1287 (2019). https://doi.org/10.1016/j.jallcom.2019.05.128
49. Y. Shadangi, V. Shivam, S. Varalakshmi, J. Basu, K. Chattopadhyay, B. Majumdar, N.K. Mukhopadhyay, Mechanically driven structural transformation in Sn reinforced Al–Cu–Fe

quasicrystalline matrix nanocomposite. J. Alloys Compd. **834**, 155065 (2020). https://doi.org/10.1016/j.jallcom.2020.155065

50. V.K. Pandey, Y. Shadangi, V. Shivam, J. Basu, K. Chattopadhyay, B. Majumdar, B.N. Sarma, N.K. Mukhopadhyay, Synthesis, characterization and thermal stability of nanocrystalline MgAlMnFeCu low-density high-entropy alloy. Trans. Indian Inst. Met. **74**, 33–44 (2021). https://doi.org/10.1007/s12666-020-02114-4
51. R. Rawat, B.K. Singh, A. Tiwari, N. Arun, A.P. Pathak, Y. Shadangi, N.K. Mukhopadhyay, S.R. Nelamarri, S.V. Rao, A. Tripathi, Formation of Cu-Ni enriched phases during laser processing of non-equiatomic AlSiCrMnFeNiCu high entropy alloy nanoparticles. J. Alloys Compd. **927**, 166905 (2022). https://doi.org/10.1016/j.jallcom.2022.166905
52. M. Raviathul Basariya, V.C. Srivastava, N.K. Mukhopadhyay, Microstructural characteristics and mechanical properties of carbon nanotube reinforced aluminum alloy composites produced by ball milling. Mater. Des. **64**, 542–549 (2014). https://doi.org/10.1016/j.matdes.2014.08.019
53. Z. Yuan, W. Tian, F. Li, Q. Fu, X. Wang, W. Qian, W. An, Effect of heat treatment on the interface of high-entropy alloy particles reinforced aluminum matrix composites. J. Alloys Compd. **822**, 153658 (2020). https://doi.org/10.1016/j.jallcom.2020.153658
54. N. Wang, B. Wu, W. Wu, J. Li, C. Ge, Y. Dong, L. Zhang, Y. Wang, Microstructure and properties of aluminium-high entropy alloy composites fabricated by mechanical alloying and spark plasma sintering. Mater. Today Commun. **25**, 1–8 (2020). https://doi.org/10.1016/j.mtcomm.2020.101366
55. Y. Shadangi, V. Shivam, K. Chattopadhyay, N.K. Mukhopadhyay, Powder metallurgical processing of Sn-reinforced Al-Cu-Fe quasicrystals : structure, microstructure and toughening behavior. J. Manuf. Mater. Process. **6**, 60–76 (2022)